Article

An Airborne Visible Light Lidar's Methodology for Clear Air Turbulence Detection Based on Weak Optical Signal

Jing Zhao [1,2] **, Xiujuan Luo** [1,*] **and Hui Liu** [1,2]

1   Xi'an Institute of Optics and Precision Mechanics, Chinese Academy of Sciences, Xi'an 710119, China; zhaojing2017@opt.ac.cn (J.Z.); liuhui1@opt.ac.cn (H.L.)
2   University of Chinese Academy of Sciences, Beijing 100049, China
*   Correspondence: xj_luo@opt.ac.cn; Tel.: +86-029-88887064

Abstract: A clear air turbulence (CAT) detection method using a 532 nm visible light airborne laser radar (LiDAR) system is proposed to address the urgent challenge in the aviation safety field. This method is based on the indirect detection technique of atmospheric molecular density for CAT and utilizes the strong aerosol scattering absorption characteristics of the iodine molecular 1109 absorption line to eliminate the interference of aerosol scattering and extinction on the weak molecular backscattering signal caused by CAT. This enables CAT detection under conditions where traditional ultraviolet LiDAR systems fail to function properly due to aerosol presence. The influence of axial wind speed and atmospheric temperature variations on the molecular backscattering spectrum in the aircraft flight path is studied, and a formula for vertical wind speed inversion in the CAT field is derived. The 532 nm airborne LiDAR CAT detection theoretical model and system architecture are presented. Through simulation analysis, the CAT detection range of the visible light LiDAR system is evaluated under different aircraft cruising altitudes and turbulence intensities. The results indicate that, with the proposed LiDAR system, the aerosol scattering influence can be effectively suppressed, and CAT can be detected up to 7 km for light-to-moderate turbulence and 10 km for moderate turbulence ahead of the aircraft when traditional ultraviolet LiDAR systems fail as the backscattering coefficient ratio between aerosol and molecule reaches the 10^{-1} condition. Based on this finding, a suggestion is made to construct a dual-wavelength (ultraviolet-visible) LiDAR system for CAT detection, aiming to solve the full coverage problem of CAT detection under various aerosol conditions. This study has a reference value for promoting the early resolution of CAT detection in the aviation field.

Keywords: clear air turbulence; atmospheric scattering; laser detection; laser detection

1. Introduction

Clear-air turbulence (CAT) generally refers to turbulence occurring at altitudes above 6 km and is unrelated to convective clouds [1], it does not include turbulence associated with convectively unstable boundaries and deep convection but does not exclude the presence of turbulence in non-convective clouds (often referring to roll clouds). Among atmospheric turbulence accidents, 40% are designated as caused by CAT [2]. It is a major cause of non-fatal aviation accidents, resulting in injuries to passengers and damage to aircraft structures; according to the Federal Aviation Administration (FAA), in the United States, an average of 58 passengers are injured each year, costing commercial airlines more than USD 100 million [3–5]. With the increases in global climate change and air traffic, the frequency of CAT occurrences will continue to rise, posing a significant threat to aviation safety [2,5]. In the aviation field, the remote detection of CAT atmospheric motion severity is necessary to provide sufficient time for onboard personnel to take protective measures [6]. However, CAT occurs in clear skies at high altitudes without significant microparticles (such as rain, snow, fog, or cloud condensation nuclei), making it extremely

difficult and nearly impossible to forecast using traditional methods such as weather forecasting, wind profilers, microwave radiometry, THz remote sensing, meteorological satellites, and weather radars [6,7]. Coherent Doppler LiDAR (CDL) technology and incoherent Rayleigh LiDAR technology are currently the most promising methods for active CAT detection [6,8]. In the late 1960s, with strong support from the FAA in the United States, the National Aeronautics and Space Administration (NASA) conducted flight tests on CDL systems based on different lasers, such as ruby and carbon dioxide lasers [9–11]. The results showed that CDL systems had a measurement accuracy of fewer than 1 m/s for the axial wind speed at the intermediate and low altitudes, but they were unable to achieve turbulence alerts at cruising altitudes (30–40 kft). Direct-detection Doppler wind LiDAR (DD-DWL) systems can determine the axial wind speed from molecular backscattering spectra, which can be used as an alternative to CDL systems when aerosols are absent. However, the dominant factor causing clear-air turbulence is the vertical wind speed, and there is sometimes no direct correlation between the axial and horizontal wind speeds within CAT areas [6], rendering the DD-DWL systems unable to accurately detect CAT. After many years of research, the Demonstration of LiDAR-based CAT Detection (DELICAT) project, consisting of 12 renowned European companies (including Thales and Airbus), proposed a CAT detection method based on atmospheric molecular density fluctuations and developed a high-power ultraviolet LiDAR system. Flight test results in 2013 showed that, under low aerosol conditions, the system could detect light-to-moderate CAT and moderate CAT up to 5 km and 10 km ahead of the aircraft, respectively [8]. This method has become a promising approach for remote CAT detection, but to ensure that there is enough CAT prewarning time, the detection distance of CAT should be at least 15 km [8], and its challenge lies in the separation of the Rayleigh scattering signal and the aerosol backscattering signal [5,6]. Studies have found that, even with ultraviolet light, aerosol backscattering can overwhelm the molecular backscattering signal changes caused by CAT, failing the detection system [8]. Through the tireless efforts of researchers, various methods, such as interferometers, and atomic and molecular filters, have been developed to remove aerosol scattering signals [12–20]. Fiocco et al. attempted to separate aerosol scattering signals from molecular Rayleigh scattering signals using Fabry–Perot interferometers [12]. C. Y. She et al. achieved atmospheric temperature detection using barium atomic filters and later conducted atmospheric parameter measurements using barium atomic and iodine molecular absorption filters [13]. Hair et al. measured tropospheric temperature at 532 nm using two iodine molecular absorption filters [14]. Studies showed that interferometer filters have a relatively lower suppression performance for aerosol scattering signals, typically in the range of 10^{-1}–10^{-3}. In contrast, atomic and molecular resonance filters exhibit stronger suppression capabilities for aerosol scattering signals, reaching levels of 10^{-5}–10^{-6}, which makes it the most ideal molecular absorption spectrum discriminator currently available. These filters have been successfully applied in spaceborne LiDAR systems, and research on these filter simulation models plays a pivotal role in the design and optimization of high-spectral-resolution LiDAR (HSRL) systems, which are anticipated to continue evolving and improving in the future, in conjunction with the characteristics of the study targets.

This paper proposes an airborne 532 nm LiDAR CAT detection method with strong aerosol interference suppression performance, which uses the existing iodine molecular absorption filters with a strong aerosol suppression performance and considers the influence of turbulence on atmospheric scattering spectra. The detection theory and system architecture are presented. Combined with simulation, the feasibility of 532 nm LiDAR for CAT detection under aerosol interference conditions is evaluated and verified, which provides a theoretical basis for airborne visible light LiDAR CAT detection technology.

2. Theories and Methods

2.1. Principle of CAT Detection

CAT is generated as a result of the saturation and breaking of gravity waves (GWs). This intricate gravity wave field is associated with terrain, convective activity induced by thunderstorms, and atmospheric layer shear instability. Vertical wind speed, which is the main velocity component causing aircraft bumps in the CAT region, is 10 times stronger than the aircraft acceleration response caused by axial/horizontal wind speeds [6] and is a key factor of LiDAR CAT detection, but it cannot be obtained using Doppler anemometry. Thus, to facilitate CAT detection by LiDAR, when the Richardson exponent *Ri* takes its critical value of 0.25, based on the definition of the atmospheric Brunt–Väisälä angular frequency *N*, Feneyrou et al. demonstrated the link between the atmospheric temperature fluctuation ΔT, the density fluctuation $\Delta \rho$, and the vertical velocity variation *w* [6,21]:

$$\frac{\Delta \rho(x)}{\rho} = -\frac{\Delta T(x)}{T} = \frac{N}{g}w(x) \tag{1}$$

where *g* is the gravity acceleration; and *T* and ρ are atmospheric temperature and density, respectively. In the Brunt–Väisälä angular frequency $N = [(g/\theta)/(\Delta\theta/\Delta z)]$, θ is the potential temperature and Δz is the vertical displacement of a fluid particle linked with the density and temperature fluctuations. In the case of GWs and turbulence, the vertical kinetic energy $1/(2w^2)$ is approximately equal to the potential energy $1/(2N^2\Delta z^2)$. Hence, it is possible to identify $\Delta z = w/N$. The typical value of *N* is 0.01 rad/s in the troposphere and 0.02 rad/s in the stratosphere, resulting in an oscillation of about 5–10 min. Therefore, in the tens of seconds, the atmospheric density fluctuation can be considered to be "frozen", which provides the time for long-range CAT detection.

As can be seen from Equation (1), the relative density fluctuation $|\Delta\rho/\rho|$ is related to wind speed *w* and frequency *N*. The larger the *w* and *N* are, the more obvious the atmospheric density fluctuation $\Delta\rho/\rho$ is, and the more favorable the conditions are for turbulence detection. According to the LiDAR equation, the atmospheric backscattering intensity is proportional to the atmospheric density. Hence, the *w* in the CAT region obtained using the atmospheric backscatter signal intensity $S_\pi(x)$ detected at a distance *x* ahead of the aircraft by LiDAR is:

$$w(x) = \frac{g}{N}\frac{\Delta\rho}{\rho} = \frac{g}{N}\frac{\Delta\beta_\pi}{\beta_\pi} \approx \frac{g}{N}\left[1 - \frac{S_{\pi,0}(x)}{S_\pi(x)}\right] \tag{2}$$

where β_π is the molecular Rayleigh backscattering coefficient; $\Delta\beta_\pi$ is the change in Rayleigh backscattering coefficient caused by density fluctuation $\Delta\rho$. $S_{\pi,0}(x)$ is the average number of scattered echo photons at a distance of *x*.

In the CAT region, vertical wind speeds usually have an irregular distribution. Based on the relevant meteorological theories and a large amount of measurement data, for the medium-scale and large-scale turbulence, not the small-scale turbulence, Von Kármán derived a more accurate velocity spectral function for turbulent fields with high-frequency components. The turbulent wind speed distribution can be simulated using the Von Kármán velocity spectral function. This spectral function satisfies both Kolmogorov's condition and the actual turbulence situation [21–23]. According to the definition, turbulence is assumed to be frozen, and the vertical velocity spectrum is:

$$\begin{aligned}\Phi_{gg}(\omega) &= H_w(\omega) \cdot conj[H_w(\omega)] \\ &= \frac{\sigma_w^2 L_w}{\pi V}\frac{1 + \frac{8}{3}\left(aL_w\frac{\omega}{V}\right)^2}{\left[1 + \left(aL_w\frac{\omega}{V}\right)^2\right]^{\frac{11}{6}}}\end{aligned} \tag{3}$$

$$H_w(\omega) = \sqrt{\frac{\sigma_w^2 L_w}{\pi V}}\frac{1 + 2.7478jL_w\frac{\omega}{V} - 0.3398\left(L_w\frac{\omega}{V}\right)^2}{1 + 2.9958jL_w\frac{\omega}{V} - 1.9754\left(L_w\frac{\omega}{V}\right)^2 - 0.1539j\left(L_w\frac{\omega}{V}\right)^3} \tag{4}$$

where *conj* stands for conjugate; $H_w(\omega)$ is the shaping filter for turbulent velocity simulation; $a = 1.339$; ω is the angular frequency; σ_w is the root-mean-square (RMS) of the vertical wind speed, which determines the turbulence intensity; V is the aircraft speed; L_w is the turbulence out-scaling, which in the field of aeronautics and aerodynamics is constant for altitudes greater than 2000 ft. For the Von Kármán spectral function, from the military references, the recommended $L_w = 2500$ ft, and for a typical transonic, the value of L_w/V is 3 s [21].

The vorticity dissipation rate (EDR) is a key parameter related to flight safety and meteorological conditions, which is used to describe the degree of atmospheric turbulence during flight. The International Civil Aviation Organization (ICAO) supports the EDR used to accurately classify the turbulence intensity levels. The correspondence between the turbulence intensity levels and the EDR in CAT perceived by the flight crew [8] is shown in Table 1.

Table 1. Correspondence between CAT intensity levels and *EDR*.

$EDR/\mathrm{m^{2/3} \cdot s^{-1}}$	Levels
<0.1	None
0.1–0.4	Light
0.4–0.7	Moderate
>0.7	Severe

The relationship between vertical wind speed RMS σ_w and the *EDR* is [24]:

$$EDR = \left(0.78 \frac{1}{L_w^{2/3}} \cdot \sigma_w^2\right)^{\frac{1}{2}} \tag{5}$$

Using Equation (6) and the relationships between the *EDR* and the CAT intensity levels listed in Table 1, the σ_w corresponding to different CAT intensities can be obtained. After calculation, for moderate CAT detection, the LiDAR has to detect relative atmospheric density fluctuations $|\Delta\rho/\rho|$ or relative molecular backscattering signal fluctuations $|\Delta\beta/\beta_\pi|$ of 4.2×10^{-3}–1.48×10^{-2}, which implies that, if the aerosol backscattering light intensity is stronger than the molecular backscattering light intensity fluctuation at the above level, it will have an impact on the correctness of the system detection results. Therefore, during CAT detection, it is necessary to reduce the aerosol backscattering signal intensity below the above molecular backscattering intensity fluctuation level.

2.2. Visible Airborne LiDAR CAT Detection Principle

In the atmosphere, molecules and aerosol particles have different random motion speeds, and the Rayleigh scattering spectra will undergo Doppler broadening when the laser encounters them, which results in the spectral widths being much wider than the emission laser spectral widths; in contrast, the Mie scattering spectral widths change insignificantly, and keep the same narrow spectral width with the emission laser.

Based on differences in the above backscattering spectral width and using a properly designed narrow-band spectral filter, the homogeneous and stable molecular backscattering signals can be separated from the non-homogeneous aerosol backscattering signals. It was found that the iodine molecular 1109 absorption line [14] has good trapezoidal symmetry and bottom flatness, and the absorption peak is stably located in the vicinity of 532 nm, which can reduce the Doppler shift effect (caused by axial wind speed) on the transmitted light intensity of the iodine molecular absorption filter (IMAF), and is good for the vertical wind speed detection accuracy in the CAT. Moreover, according to the atmospheric Rayleigh scattering principle, the long-wavelength laser is more sensitive to turbulence intensity and other parameter changes, and for a reasonably designed system, the laser wavelength near 532 nm considers the scattering and transmitting ability, which is conducive to the CAT detection distance improvement. Therefore, a 532 nm pulsed Nd: YAG laser and an IMAF

are selected to suppress the Mie scattering signal of the aerosol and realize the detection of the weak signal of the moderate CAT.

The iodine molecular 1109 absorption line, with its strong absorption, wide absorption range, its peak, and width, can be designed by adjusting the operating temperature, pressure, and length. According to the simulation model given in the literature [18], the IMAF principle is shown in Figure 1. From Figure 1a, when the IMAF length is 15 cm, the iodine finger temperature is 65 °C, the pressure is 2 Torr, and the absorption line width is about 2 GHz; meanwhile, the maximum transmittance is of approximately 0.8, and the minimum transmittance is about 1×10^{-5}. The CAT detection principle based on the IMAF is shown in Figure 1b. Due to the iodine molecule's strong aerosol backscattering absorption property at 532 nm, without axial wind speed interference, when the atmospheric backscattered signal generated by the 532 nm pulsed laser passes through the IMAF, the aerosol backscattering signal located near the center frequency is suppressed, and the detector receives part of the Rayleigh backscattered signal. Thus, it is necessary to place the Rayleigh–Mie scattering spectral in the middle of the iodine molecule 1109 absorption line, to strongly suppress the aerosol scattering signal and obtain the turbulence-related Rayleigh backscattered light intensity changes.
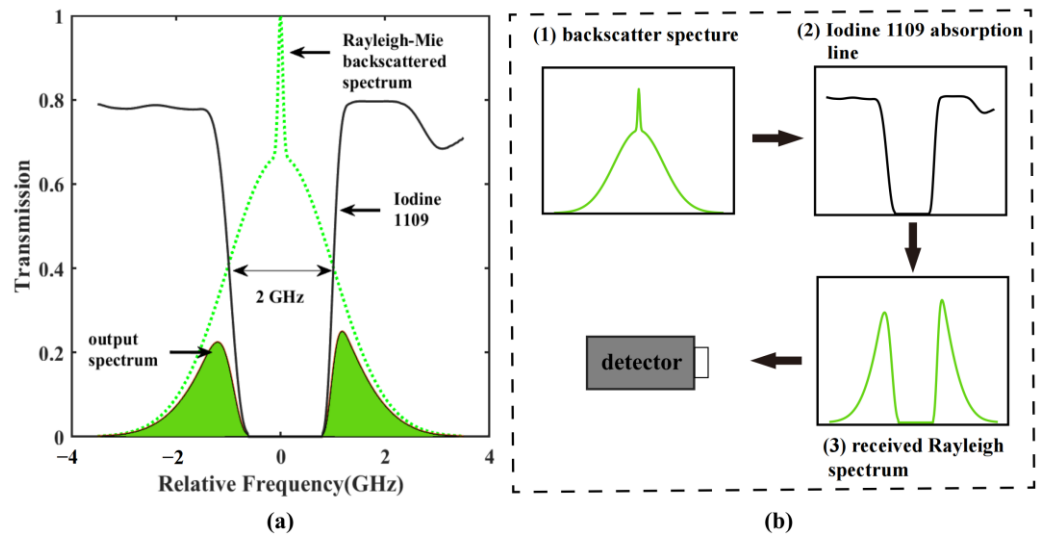

Figure 1. Schematic diagram of IMAF. (**a**) Iodine molecule 1109 absorption line and atmospheric backscattering spectral. (**b**) Suppression principle of aerosol backscattered light by the IMAF.

The transmittance of the molecular and aerosol backscattered lights passing through the IMAF, respectively, can be expressed as:

$$F_M(T, v) = \int R_M(T, v, \nu) t_{1109}(\nu) d\nu \tag{6}$$

$$F_A(v) = \int R_A(v, \nu) t_{1109}(\nu) d\nu \tag{7}$$

where F_M is the molecular backscattered lights passing through the IMAF; F_A is the aerosol backscattered lights passing through the IMAF; t_{1109} is the IMAF transfer function; T is the atmospheric temperature; R_M and R_A are the molecular backscattering spectra and aerosol backscattering spectra, respectively; v is the axial wind speed; and ν is the center frequency of the emitted laser.

The atmospheric Rayleigh–Mie backscattering spectrum in Figure 1a underscores the Doppler shifting and broadening being affected by the axial wind speed and atmospheric

temperature. The transmittances R_M and R_A, respectively, are related to the temperature and axial wind speed as [25]:

$$R_M(T, v, \nu) = \sqrt{\frac{M\lambda^2}{8\pi k_B T}} \exp\left[-\frac{M\lambda^2\left(\nu - \frac{2v}{\lambda}\right)^2}{8k_B T}\right] \tag{8}$$

$$R_A(v, \nu) = \sqrt{\frac{4\ln 2}{\pi \Delta\nu}} \exp\left[-\frac{4\ln 2\left(\nu - \frac{2v}{\lambda}\right)^2}{\Delta\nu^2}\right] \tag{9}$$

where k_B is the Boltzmann constant; M is the average mass of atmospheric molecules; $\Delta\nu$ is the spectral width of the emitted laser; λ is the laser wavelength; and $2v/\lambda$ is the Doppler shift induced by the axial wind speed.

Due to the non-complete symmetry of the IMAF transfer curve, the transmittances F_M and F_A will be affected by the atmospheric axial wind speed and temperature, which have an impact on the vertical wind speed inversion results. Hence, the atmospheric temperature and axial wind speed effects on the transmittances F_M and F_A need to be evaluated. According to Equations (6)–(9), the transmittance F_M for molecular backscattered light under the different temperatures and axial wind speeds is shown in Figure 2. It can be seen that the transmittance F_M is approximately 0.25; both the temperature and axial wind speed will affect the F_M, and the larger the temperature and axial wind speed are, the larger the F_M is; in contrast, the transmittance F_M is more affected by temperature, and increases in a manner that is directly proportional to the temperature increase.
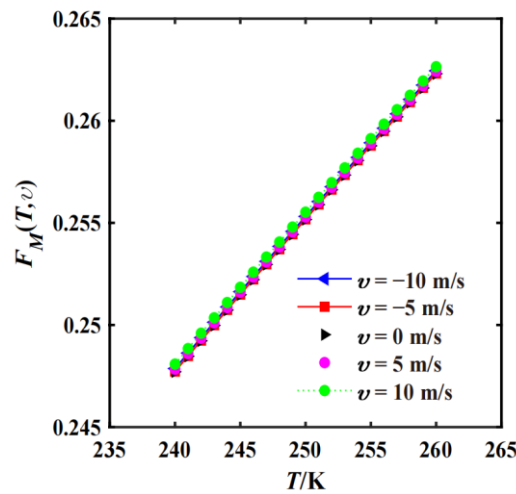

Figure 2. Changes in transmittance $F_M(T,v)$ of iodine molecules under different atmospheric temperatures and axial wind speeds.

Polynomial fitting to the transmittance change induced by temperature and axial wind speed changes in Figure 2, the transmittance F_M of the IMAF versus the temperature T and axial wind speed v which can be approximated as:

$$F_M(T, v) \approx (a_1 \cdot |v| + a_2) \cdot T^2 + (a_3 \cdot |v| + a_4) \cdot T + (a_5 \cdot |v| + a_6) \tag{10}$$

where $a_1{\sim}a_6$ are the curve fitting coefficients, $a_1 \approx 3.0698 \times 10^{-10}$, $a_2 \approx -1.5970 \times 10^{-6}$, $a_3 \approx -2.7266 \times 10^{-7}$, $a_4 \approx 0.0015$, $a_5 \approx 7.6198 \times 10^{-5}$, and $a_6 \approx -0.0271$. Using the above equations, the backscattered light intensity changes caused by the IMAF absorbance can be corrected when the temperature T and axial wind speed v are known. Correction for the change in scattered light intensity caused by the change in filter transmittance.

The changes in the effects of atmospheric temperature and axial wind speed on the transmittance ratio F_A/F_M of IMAF are shown in Figure 3. The F_A/F_M, up to 10^{-5} orders of magnitude at lower levels, is much smaller than the relative atmospheric density

fluctuation $|\Delta\rho/\rho|$ level (10^{-3}–10^{-2}) caused by moderate CAT. And, F_A/F_M decreases with the increases in both temperature and axial wind speed. These phenomena indicate that the aerosol backscattering intensity output from the IMAF is negligible, and enlarging the temperature and axial wind speed may be beneficial to the extraction of Rayleigh scattering signals by IMAF.
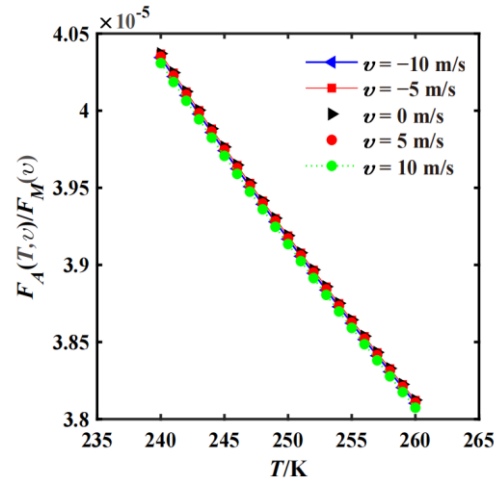

Figure 3. Changes in transmittance $F_M(T,v)/F_A(v)$ of IMAF under different atmospheric temperatures and radial wind speeds.

In the process of an airplane flying along a specific route with speed *V*, assuming its flight attitude and speed are unchanged, the frequency of the onboard LiDAR detecting the atmosphere in front of the airplane on the flight route is PRF. Between two adjacent laser shots, the distance of the airplane's advance is V/PRF. In this detection mode, a large number of pulse-echo signals are needed for cumulative averaging to obtain a good signal-to-noise ratio. Therefore, there needs to be an integrated distance *L* for the cumulative averaging of the scattered echo signals, and the actual detection distance *R* is the distance after the end of the integration distance *L*. If N_s laser pulses are emitted by the LiDAR within the integration distance, the sum of the N_s atmospheric backscattered signals output from the IMAF at a distance *x* is:

$$
\begin{aligned}
S_\pi(x) &= S_{\pi,A}(x) \cdot F_A(v(x)) + S_{\pi,M} \cdot F_M(T(x),v(x)) + B \\
&= \sum_{i=1}^{Ns} \frac{\eta\chi P_0 \lambda A T_1 T_2 \Delta\tau}{2h(x-iV/PRF)^2} [\beta_a(x) \cdot F_A(v(x)) + \beta_m(x) \cdot F_M(T(x),v(x))] \\
&\quad \times \exp\left\{ -2 \int_0^{x-iV/PRF} [\alpha_a(r) + \alpha_m(r)] dr \right\} + B
\end{aligned}
\tag{11}
$$

where $S_{\pi,A}(x)$ and $S_{\pi,M}(x)$ are the intensity of the aerosol and molecular backscattered light received by the LiDAR at a distance *x* ahead of the aircraft, respectively; *i* is the number of laser shots; η is the detector quantum efficiency; χ is the filling factor; P_0 is the laser power; *A* is the effective receiving area of the receiving telescope; T_1 and T_2 are the transmissions of the emission and the collection, respectively; $\Delta\tau$ is the signal acquisition time; *h* is the Planck's constant; *B* is the photon noise (including sunlight participation, dark current, and thermal noise, etc.), which obeys the characteristics of the Poisson distribution in atmospheric LiDAR detection; β_a and β_m are the aerosol and molecular backscattering coefficients, respectively; and α_a and α_m are the aerosol and molecular extinction coefficients, respectively. α_a/β_a is the aerosol extinction scattering ratio, which is related to the laser wavelength and the scale of the aerosol, etc., and when $\lambda = 532$ nm, $\alpha_a/\beta_a = 50$ Sr; α_m/β_m is the air molecules' extinction scattering ratio, which has a value of $8\pi/3$.

According to the Rayleigh scattering theory, the average molecular backscattering coefficient $\beta_{m,0}$ can be calculated by the detected air pressure and temperature data on the airplane route. The average Rayleigh scattered echo photon number $S_{\pi,0}(x)$ is:

$$S_{\pi,0}(x) = \sum_{i=1}^{Ns} \frac{\eta \chi P_0 \lambda A T_1 T_2 \Delta \tau}{2h(x-iV/PRF)^2} \beta_{m,0} \times \exp\left\{ -2 \int_0^{x-iV/PRF} \left[\alpha_a(r) + \frac{8\pi}{3}\beta_{m,0} \right] dr \right\} \quad (12)$$

Using Equation (2) and neglecting the influence of axial wind speed on atmospheric backscattered light intensity, Equation (11) can be expressed as:

$$
\begin{aligned}
S_{\pi}(x) \approx & \sum_{i=1}^{Ns} \frac{\eta \chi P_0 \lambda A T_1 T_2 \Delta \tau}{2h(x-iV_a/PRF)^2} [\beta_m + \Delta\beta_m(x)] \cdot F_M(T_0 + \Delta T(x), 0) \\
& \times \exp\left\{ -2 \int_0^{x-iV/PRF} [\alpha_a(r) + \alpha_m(r)]dr \right\} + B \\
\approx & \sum_{i=1}^{Ns} \frac{\eta \chi P_0 A T_1 T_2 \Delta \tau}{2h(x-iV/PRF)^2} \beta_m \exp\left\{ -2 \int_0^{x-iV/PRF} [\alpha_a(r) + \alpha_m(r)]dr \right\} \times \left[1 + N\frac{w(x)}{g} \right] \\
& \times \left\{ a_2 T_0^2 \left[1 - N\frac{w(x)}{g} \right]^2 + a_4 T_0 \left[1 - N\frac{w(x)}{g} \right] + a_6 \right\} + B
\end{aligned}
\quad (13)
$$

Neglecting the higher-order power terms of $|N{\cdot}w(x)/g|$ in Equation (13), when the mean atmospheric temperature T_0 and the molecular Rayleigh backscattered echo photon number $S_{\pi,0}(x)$ are known, at the cruising altitude, the vertical wind speed w distribution in the CAT field obtained by Equation (13) is:

$$w(x) \approx \frac{g}{N} \times \frac{\frac{S_{\pi}(x)}{S_{\pi,0}(x)} - a_2 T_0^2 - a_4 T_0 - a_6}{a_6 - a_2 T_0^2} \quad (14)$$

By processing the distance information in Equation (14) and subtracting the distance x from the integral distance L, the vertical wind speed distribution with the detection distance R can be obtained.

3. System Design

Based on the above theories, the 532 nm airborne LiDAR CAT detection system architecture is designed, as shown in Figure 4. Channel 1 is used to detect the total intensity of atmospheric aerosol and molecular backscattering signals, and channel 2 is used to suppress aerosol backscattering signals. To improve the CAT detection performance, an avalanche photodiode (APD) is chosen as the detector in the system, which has a high quantum conversion efficiency in the visible wavelength band.

To reduce the flight speed interference on the CAT detection results, the optical and acoustic transducer frequency shifter is used in the system to compensate for the frequency change of the scattering spectrum center caused by the aircraft speed and stabilize it at the center of the IMAF absorption line. During the aircraft flight, the LiDAR-emitted laser encounters atmospheric aerosols and molecules and undergoes Mie scattering and Rayleigh scattering, respectively. The atmospheric backscattered signal arrives at the detection system and is proportionally divided into two parts: one part is directly received by the APD1 and the other part first passes through a narrow-band filter to reduce the interference of the background sunlight, then sent to the IMAF to remove the Mie scattering signal of the aerosols, and then received by the APD2. Then, the number of scattered echo photons detected by all channels is sent to the computer for signal storage and processing.
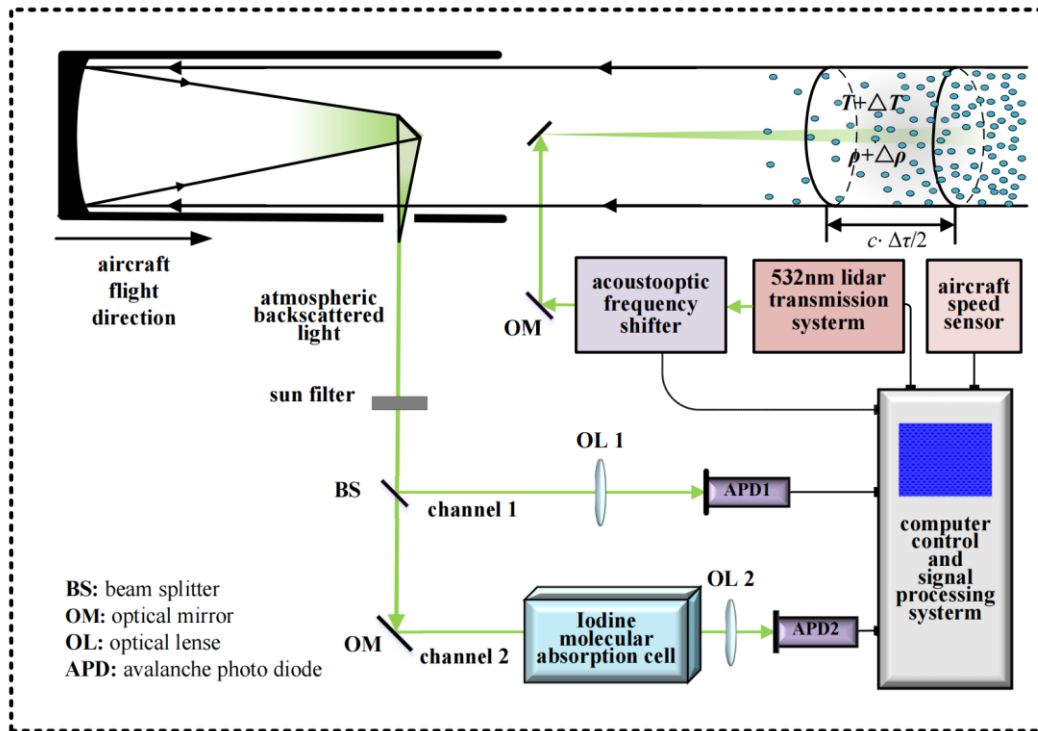
Figure 4. Simplified synopsis of airborne LiDAR CAT detection system.

When the molecular backscattered light intensities detected by the APD of channels 1 and 2 are equal, the distribution of the aerosol backscattering coefficients β_a for the flight path can be obtained using the ratio of the final output scattered light intensities of channels 1 and 2. Assuming that the average transmittance of the IMAF is $F_M(T_0, 0)$ and the total light intensity input to channels 1 and 2 is S_{all}, the scattered light intensities S_1 and S_2 input to channels 1 and 2 are denoted as:

$$S_1 = \frac{F_M(T_0, 0)}{1 + F_M(T_0, 0)} S_{all} \tag{15}$$

$$S_2 = \frac{1}{1 + F_M(T_0, 0)} S_{all} \tag{16}$$

By substituting β_a and the mean molecular backscattering coefficient $\beta_{m,0}$ into Equation (11), the mean Rayleigh scattered return photon number $S_{\pi,0}(x)$ is obtained by calculation. In turn, the vertical wind speed $w(x)$ distribution in the CAT region is obtained from the inversion of Equation (13). Finally, the turbulence intensity is obtained from Equation (4).

The design and implementation of this system using molecular and atomic absorption filters are relatively complex, requiring the precise adjustment of filters, control system parameters, and the handling of multi-channel spectral data. It demands high requirements for system integration and operational techniques to facilitate this approach into practical applications. In the future, based on the above detection technology mechanism and system architecture, using the existing iodine molecular filter, high-power 532 nm pulse laser, narrow-spectrum sun filter, and reasonably designed turbulence generator, it will be possible to design higher-performance airborne LiDAR CAT detection systems and carry out CAT experiment verification in the laboratory.

4. Simulation and Results Analysis

Building upon the previously elucidated CAT detection model and system architecture, and considering the intricate atmospheric conditions of the CAT, we incorporated extant

simulation models and relevant theoretical underpinnings to construct a comprehensive simulation model, which is convenient for meticulous validation through a computer. Within this model, we amalgamated elements from the atmospheric density fluctuation-based CAT detection model [21], the iodine molecular absorption spectral line model, models for atmospheric aerosol and molecular backscattering spectral distribution, as well as the Doppler and broadening effects of atmospheric wind speed and temperature variations on backscattering spectra, which were all integrated within the LiDAR equations.

The simulation flow of the 532 nm airborne LiDAR CAT detection system is shown in Figure 5. First, set the CAT intensity level and scale, and calculate the corresponding RMS σ_w of the vertical wind speeds according to Table 1 and Equation (5). Based on the Monte Carlo method, the Gaussian white noise with zero mean and unit variance is passed through the shaping filter $H_w(\omega)$ obtained from the velocity spectral function $\Phi_{gg}(\omega)$, and the initial vertical and axial wind speed is generated so that it is consistent with turbulence characteristics. The correlation function $f_1(R)$ calculated from the actual vertical wind speed is compared with the theoretical correlation function $f_0(R)$ to modify the vertical wind speed amplitude. When $f_1(R)$ and $f_0(R)$ match, the vertical wind field distribution matching the target intensity is obtained, where $f_0(R)$ is the Fourier transform of $\Phi_{gg}(\omega)$ [21–23]. Then, set the mean atmospheric temperature T, pressure P, and Brundt–Väisälä frequency N at the flight altitude, and obtain the atmospheric density and temperature variations related to the vertical wind speed using Equation (1) to establish a CAT model. Subsequently, set the parameters of the IMAF, LiDAR, and sun filter, according to the airborne LiDAR CAT detection principles and photon noise characteristics, simulate the LiDAR-detected atmospheric backscattered echo signals, and feed the scattered echo signals into the IMAF to filter out the aerosol backscattered signals. Then, using Equation (14), invert the vertical wind speed distribution in the CAT field from the molecular backscattered signal intensity output from the IMAF, and then compare the results of the vertical wind speed inversion w_1 with the initial vertical wind speed w_0 to verify the detection model correctness. Finally, compute and analyze the correlation between the vertical wind speed inversion results and the initial vertical wind speed, and take the detection distance corresponding to a correlation coefficient of 0.5 as the maximum detection distance.

In the simulation, assume that the airplane attitude does not change during the leveling phase and that the CAT is an isotropic turbulence. The backscattering coefficients and extinction coefficients of the atmospheric aerosols and molecules at different altitudes can be calculated according to the literature [26]. For the 532 nm laser, the aerosol backscattering coefficient can be set to vary randomly between 0 and 0.75 times the molecular Rayleigh backscattering coefficient according to the literature [8]. The parameters of the 532 nm airborne LiDAR system used in the simulation model are shown in Table 2.

In LiDAR detection mode, with the increase in the integration distance, the detection distance gradually increases to a certain level and does not increase anymore. The Brundt–Väisälä period of a stable atmosphere is usually 300 s [21], which is much longer than the 40 s flight time; thus, a 10 km integration distance is used to guarantee a sufficient signal accumulation time. To better detect more hazardous low-frequency turbulence for airplanes, a theoretically used distance resolution is 100 m. In the theoretical study of CAT detection, to quantify the effect of different parameters on the CAT detection distance, Feneyrou et al. proposed the criterion of the correlation coefficient 0.5 [21], which defines the maximum detection distance R as the detection distance corresponding to a correlation coefficient of 0.5 between the vertical wind speed detection result w_1 and the initial vertical wind speed w_0 (obtained by the von Kármán velocity spectrum).
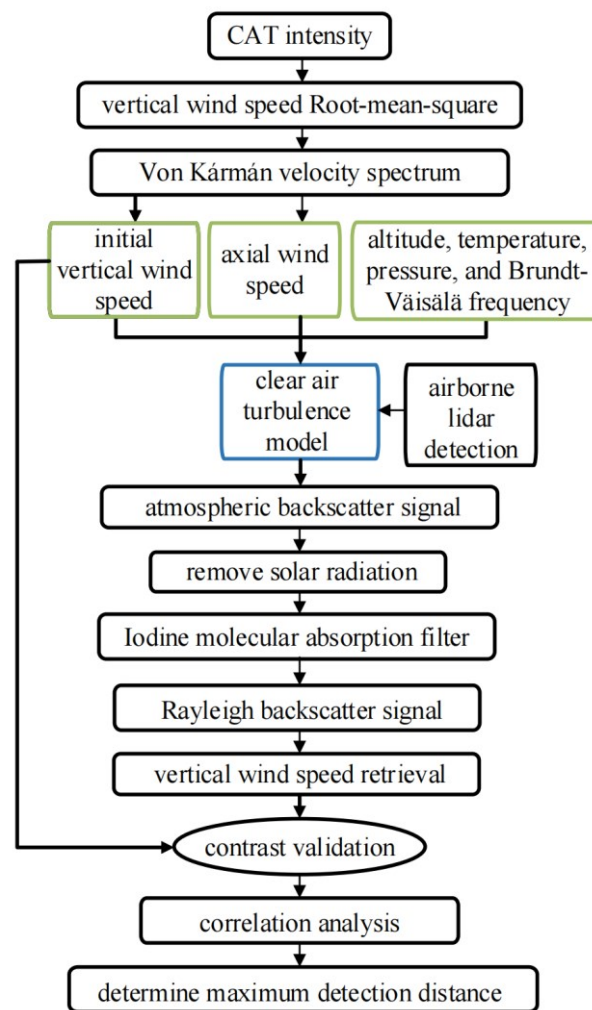
Figure 5. Simulation flow of airborne visible light LiDAR for CAT detection.

Table 2. Parameters of clear air turbulence detection system.

Parameter	Value
CAT level	Moderate
Aircraft speed	$250 \text{ m} \cdot \text{s}^{-1}$
Integration distance	10 km
Distance resolution	100 m
Brunt–Väisälä frequency	$0.01 \text{ rad} \cdot \text{s}^{-1}$
Laser pulse energy	230 mJ
Pulse length	8 ns
Repetition rate	100 Hz
Telescope diameter	140 mm
Field of view	0.53 mrad
Sun filter bandwidth (FWHM)	0.5 nm
Detector quantum efficiency	0.75
Overall optical efficiency	0.36
Solar background level	$300 \text{ W} \cdot \text{m}^{-2} \cdot \text{sr}^{-1} \cdot \text{μm}^{-1}$

An example of the detection capability for a 355 nm airborne LiDAR system (with a laser energy of 85 mJ and a detector quantum efficiency of 0.3) and a 532 nm airborne LiDAR system is given below. The maximum cruise altitude is set to $H = 12.6$ km, the Brunt–Väisälä frequency is set to $N = 0.01$ rad s^{-1}, and the CAT intensity level is light to moderate (EDR = 0.4 m$^{2/3}$ s^{-1}). The comparison results between the vertical wind speed

inversion result w_1 versus the initial vertical wind speed w_0 for the 532 nm airborne LiDAR and the 355 nm airborne LiDAR are shown in Figure 6. From Figure 6a, the 355 nm airborne LiDAR system will be influenced by random aerosol backscattering signals, the obtained vertical wind speed inversion result w_1 is larger than the initial vertical wind speed w_0, and it is almost impossible to recognize and extract the CAT intensity distribution information; whereas, from Figure 6b, the 532 nm airborne LiDAR system, in the range of the distance $R < 7$ km, obtains the vertical wind speed inversion result w_1, which is consistent with the initial vertical wind speed w_0. The 532 nm airborne LiDAR system has the effective suppression ability for strong aerosol backscattering interference, which can identify the vertical wind speed distribution in the turbulent region and realize CAT detection.
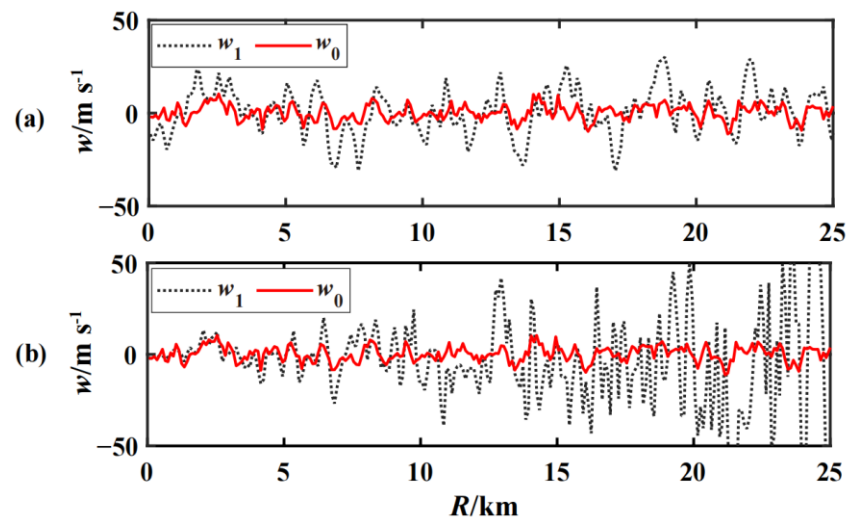
Figure 6. Comparison of vertical wind speed inversion results w_1 with the initial vertical wind speed w_0: (**a**) 355 nm airborne LiDAR; and (**b**) 532 nm airborne light LiDAR.

Then, calculate the correlations to the w_1 and w_0 in Figure 7, and the vertical wind speeds' correlation coefficients' distribution comparison of 355 nm and 532 nm airborne LiDAR systems with a distance of R is obtained, as shown in Figure 7. For the 355 nm LiDAR system, the correlation coefficient between w_1 and w_0 is less than 0.5; hence, the detection distance R is 0. For the 532 nm LiDAR system, the correlation coefficient between the calculated w_1 and w_0 decreases with the increase in the distance, and the corresponding detection distance R at 0.5 is about 7 km.
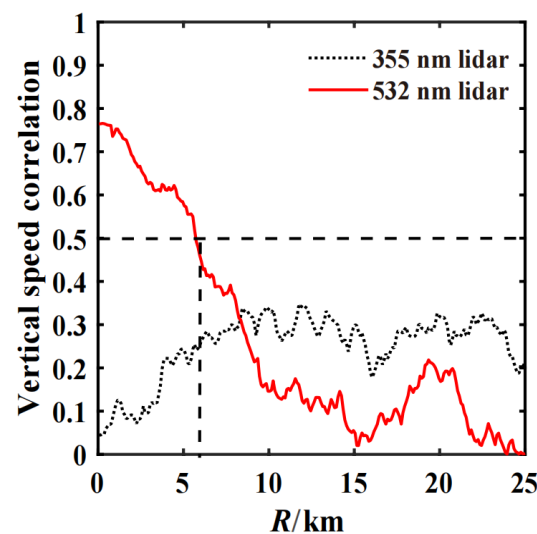
Figure 7. The impact of different LiDAR systems on the vertical speed correlation.

Each set of parameters undergo 150 independent repetitions. After statistical averaging, for different CAT intensities and atmospheric Brunt–Väisälä frequency N conditions, the variation in the detection range R of the airborne 532 nm LiDAR system with an altitude of H is obtained, as shown in Figure 8. The detection range R is enlarged with the increase in CAT intensity and frequency N. In the cruising altitude from 6 km to 12.6 km, R decreases with the increase in H, and the maximum cruising altitude $H = 12.6$ km corresponds to the minimum R. When $H = 12.6$ km and $N = 0.01$ rad/s, it can be seen from Figure 8a that, for EDR = 0.4 $m^{2/3}$/s (light-to-moderate CAT), EDR = 0.7 $m^{2/3}$/s (moderate CAT), and EDR = 1.0 $m^{2/3}$ s^{-1} (severe CAT), the R of the LiDAR system is 7.5 km, 10.1 km, and 12.8 km, respectively. Under a larger frequency $N = 0.02$ rad s^{-1}, it is shown in Figure 8b that the R of the LiDAR system is 7.5 km, 10.1 km, and 12.8 km, respectively, for EDR = 0.4 $m^{2/3}$ s^{-1}, EDR = 0.7 $m^{2/3}$ s^{-1}, and EDR = 1.0 $m^{2/3}$ s^{-1}, R is 11.7 km, 16.0 km, and 19.2 km, respectively.
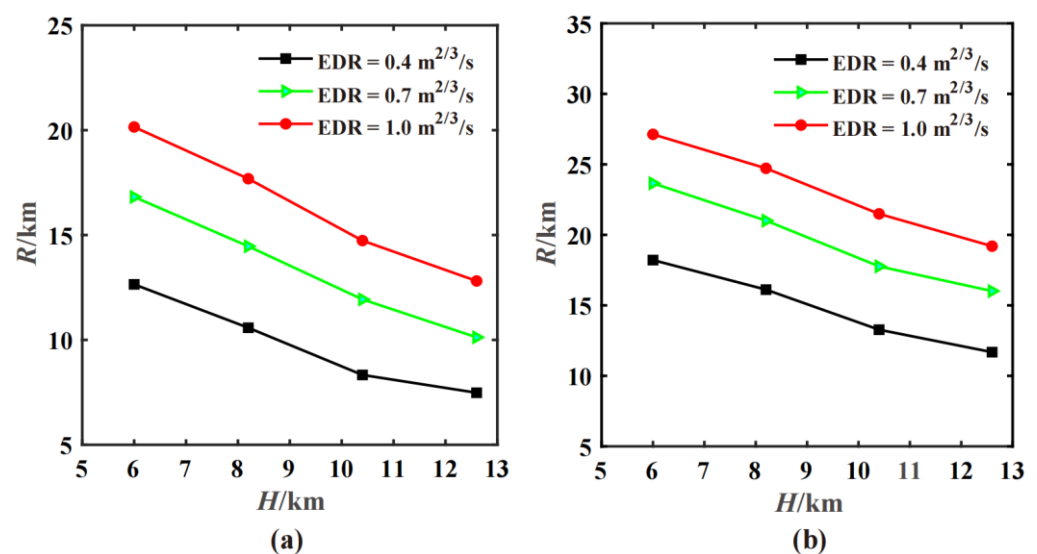

Figure 8. Changes in the detection distance of 532 nm airborne LiDAR based on the IMAF under the atmospheric Brunt–Väisälä frequency N is (**a**) 0.01 rad s^{-1} and (**b**) 0.02 rad s^{-1} conditions with a CAT intensity and altitude H.

It can be seen that, without considering the influence of the aircraft altitude and other changes in the LiDAR detection system, the 532 nm airborne LiDAR system proposed in this paper can effectively suppress the atmospheric aerosol backscattering signal, reduce the interference of the axial wind speed, and at an aircraft cruising altitude of 6–12.6 km, it can theoretically detect light-to-moderate CAT and moderate CAT at 7.5–12.6 km and 10.1–16.8 km in front of the aircraft, respectively.

5. Conclusions

This paper proposed a 532 nm airborne LiDAR CAT detection method, which incorporates the design and use of IMAF, facilitates the LiDAR suppression and detection of the aerosol backscattering intensity on the aircraft flight path, and solves the technical problem of CAT detection that cannot be realized by the traditional 355 nm airborne LiDAR under aerosol interference conditions. The simulation results show that the CAT can also be detected at a maximum cruising altitude of 12.6 km with 7 km of light-to-moderate intensity and 10 km of moderate intensity CAT in theory, which has some theoretical significance for the visible airborne LiDAR system design for remote CAT detection. However, the low energy utilization of the backscattered light from the IMAF also largely limits the CAT detection range under aerosol-sparse conditions. Based on this theoretical model, the structure and parameters of the detection system can be optimized, and a 355 nm and 532 nm dual-wavelength LiDAR system can be constructed by taking advantage of the

relatively small backscattering of the 355 nm laser, so that the distribution of aerosols on the flight paths can be monitored in real-time, and switching between the dual-wavelengths is performed according to the different aerosol conditions, realizing the full coverage problem of CAT detection under various aerosol conditions in the future. The system will improve the remote detection capability of CAT and promote the early solution of CAT detection problems.

Author Contributions: J.Z., X.L. and H.L. contributed to the project investigation, formal analysis, and the design and implementation of the proposed simulation model. J.Z. and H.L. contributed to the model verification, data analysis, and processing. X.L. and J.Z. reviewed the article and edited the manuscript together. X.L. and H.L. are project managers. All authors have read and agreed to the published version of the manuscript.

Institutional Review Board Statement: Not applicable.

Informed Consent Statement: Not applicable.

Data Availability Statement: The data presented in this study are available on request from the corresponding author.

Conflicts of Interest: The authors declare no conflict of interest.

References

1. Zhou, L.; Huang, C.F. Advances in Clear Air Turbulence Studies in Last Ten Years. *Meteorol. Sci. Technol.* **2015**, *43*, 91–96. [CrossRef]
2. Veerman, H.P.J.; Vrancken, P.; Lombard, L. Flight testing delicat—A promise for medium-range clear air turbulence protection. In Proceedings of the European 46th SETP and 25th SFTE Symposium, Luleå, Sweden, 15–18 June 2014. Available online: https://hal.science/hal-01111380 (accessed on 10 January 2019).
3. Golding, W.L. Turbulence and its Impact on Commercial Aviation. *J. Aviat./Aerosp. Educ. Res.* **2000**, *11*, 8. [CrossRef]
4. Patrick, V.; Herbst, J. Development and Test of a Fringe-Imaging Direct-Detection Doppler Wind LiDAR for Aeronautics. *EPJ Web Conf.* **2020**, *237*, 07008. [CrossRef]
5. Hu, B.Y.; Ding, G.L.; Tang, J.P. Objective Verification of Clear-Air Turbulence (CAT) Diagnostic Performance in China Using in Situ Aircraft Observation. *J. Atmos. Ocean. Technol.* **2022**, *39*, 903–914. [CrossRef]
6. Sharman, R.; Lane, T. *Aviation Turbulence: Processes, Detection, Prediction*; Springer International Publishing: Geneva, Switzerland, 2016; pp. 443–464. [CrossRef]
7. Kim, J.-H.; Park, J.-R.; Kim, S.-H.; Kim, J.; Lee, E.; Baek, S.; Lee, G. A Detection of Convectively Induced Turbulence Using in Situ Aircraft and Radar Spectral Width Data. *Remote Sens.* **2021**, *13*, 726. [CrossRef]
8. Vrancken, P.; Wirth, M.; Ehret, G.; Barny, H.; Rondeau, P.; Veerman, H.P. Airborne forwards-pointing UV Rayleigh LiDAR for remote clear air turbulence detection: System design and performance. *Appl. Opt.* **2016**, *55*, 9314–9328. [CrossRef] [PubMed]
9. Franken, P.A.; Jenney, J.A.; Rank, D.M. Airborne investigations of clear air turbulence with laser radars (Clear air turbulence detection with laser radar, noting airborne equipment and results). In Proceedings of the 8th Annual Electron and Laser Beam Symposium, Ann Arbor, MI, USA, 4 April 1966. [CrossRef]
10. Huffaker, R.M. CO_2 laser Doppler systems for the measurement of atmospheric winds and turbulence. *Atmos. Technol.* **1975**, *1*, 71–76.
11. Hannon, S.M.; Bagley, H.R.; Bogue, R.K. Airborne Doppler LiDAR turbulence detection: ACLAIM flight test results. In *Laser Radar Technology and Applications IV*; SPIE: Orlando, FL, USA, 1999. [CrossRef]
12. Fiocco, G.; Benedetti-Michelangeli, G.; Maischberger, K.; Madonna, E. Measurement of temperature and aerosol to molecule ratio in the troposphere by optical radar. *Nat. Phys. Sci.* **1971**, *229*, 78–79. [CrossRef]
13. She, C.Y.; Alvarez, R.J.; Caldwell, L.M.; Krueger, D.A. High-spectral-resolution Rayleigh–Mie LiDAR measurement of aerosol and atmospheric profiles. *Opt. Lett.* **1992**, *17*, 541–543. [CrossRef] [PubMed]
14. Hair, J.W.; Hostetler, C.A.; Cook, A.L.; Harper, D.B.; Ferrare, R.A.; Mack, T.L.; Welch, W.; Izquierdo, L.R.; Hovis, F.E. Airborne high spectral resolution LiDAR for profiling aerosol optical properties. *Appl. Opt.* **2008**, *47*, 6734–6752. [CrossRef] [PubMed]
15. Gerstenkorn, S.; Luc, P. *Atlas du Spectre d'Absorption de la Molecule d'Iode 14,800–20,000 cm^{-1}*; Editions du Centre National de la Recherche Scientifique (CNRS): Paris, France, 1978.
16. Dong, J.; Liu, J.; Bi, D.; Ma, X.; Zhu, X.; Zhu, X.; Chen, W. Optimal iodine absorption line applied for spaceborne high spectral resolution LiDAR. *Appl. Opt.* **2018**, *57*, 5413–5419. [CrossRef] [PubMed]
17. Ke, J.; Sun, Y.S.; Dong, C.Z.; Zhang, X.Y.; Wang, Z.J.; Lyu, L.Q.; Zhu, W.; Ansmann, A.; Su, L.; Bu, L.B.; et al. Development of China's first space-borne aerosol-cloud high-spectral-resolution LiDAR: Retrieval algorithm and airborne demonstration. *PhotoniX* **2022**, *3*, 17. [CrossRef]

18. Zhang, Y.; Liu, D.; Shen, X.; Bai, J.; Liu, Q.; Cheng, Z.; Tang, P.; Yang, L. Design of iodine absorption cell for high-spectral-resolution LiDAR. *Opt. Express* **2017**, *25*, 15913–15926. [CrossRef] [PubMed]

19. Forkey, J.N.; Lempert, W.R.; Miles, R.B. Corrected and calibrated I2 absorption model at frequency-doubled Nd:YAG laser wavelengths. *Appl. Opt.* **1997**, *36*, 6729–6738. [CrossRef] [PubMed]

20. Liu, D.; Zheng, Z.; Chen, W.; Wang, Z.; Li, W.; Ke, J.; Zhang, Y.; Chen, S.; Cheng, C.; Wang, S. Performance estimation of space-borne high-spectral-resolution LiDAR for cloud and aerosol optical properties at 532 nm. *Opt. Express.* **2019**, *27*, A481–A494. [CrossRef] [PubMed]

21. Feneyrou, P.; Lehureau, J.C.; Barny, H. Performance evaluation for long-range turbulence-detection using ultraviolet LiDAR. *Appl. Opt.* **2009**, *48*, 3750. [CrossRef] [PubMed]

22. Yang, S.B.; Wang, L.B. Analysis of Airworthiness Regulations of Gust and Turbulence Loads for Civil Aircraft. *Civ. Aircr. Des. Res.* **2016**, *121*, 48–53. [CrossRef]

23. Gage, S. Creating a unified graphical wind turbulence model from multiple specifications. In Proceedings of the American Institute of Aeronautics and Astronautics (AIAA) Modelling and Simulation Technologies Conference and Exhibit, Austin, TX, USA, 11–14 August 2003; p. 5529. [CrossRef]

24. Cornman, L.B.; Morse, C.S.; Cunning, G. Real-time estimation of atmospheric turbulence severity from in-situ aircraft measurements. *J. Aircr.* **1994**, *32*, 171–177. [CrossRef]

25. Shen, F.; Shu, Z.; Sun, D.; Wang, Z.; Xue, X.; Chen, T.; Dou, X. Wind retrieval algorithm of Rayleigh Doppler lidar. *Acta Phys. Sin.* **2011**, *60*, 192–198.

26. Ji, C.L.; Zhou, J. Simulation of Signal and Signal-to-noise Ratio Received by an Airborne Dual-wavelength Mie LiDAR. *J. Atmos. Environ. Opt.* **2008**, *3*, 250–261. Available online: https://kns.cnki.net/kcms/detail/detail.aspx?FileName=GXXB200106019&DbName=CJFQ2001 (accessed on 22 June 2020).